Charles University in Prague
Faculty of Mathematics and Physics

DIPLOMA THESIS

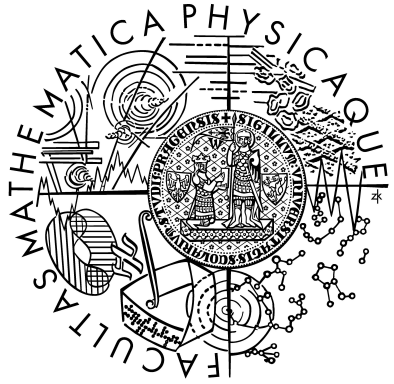

Aivaras Žukauskas

Detector for double beta decay investigation

Institute of Particle and Nuclear Physics

Supervisor: Ing. Vít Vorobel, Ph.D.
Study programme: Physics
Study field: Nuclear and Subnuclear Physics

Acknowledgements

Firstly, I want to thank to my supervisor Vít Vorobel for the leading, help and advice over the time I've been working on this subject. A big thank belongs to Benton Pahlka and Viktor Pěč for their continuous support in optical photon simulations and programming.
Finally, I would like to thank to all professors of Institute of Particle and Nuclear Physics whom I met during my studies for their patience, tolerance and shared knowledge.

Prohlašuji, že jsem svou diplomovou práci napsal samostantně a výhradně s použitím citovaných pramenů. Souhlasím se zapůjčováním práce.

I declare that I wrote my diploma thesis independently and exclusively with the use of the cited sources. I agree with lending the thesis.

Prague, 8th August 2008 Aivaras Žukauskas

Contents

List of Figures

List of Tables

Název práce: Detektor pro studium dvojného beta rozpadu

Autor: Aivaras Žukauskas

Katedra (ústav): Ústav částicové a jaderné fyziky

Vedoucí diplomové práce: Ing. Vít Vorobel, Ph.D.

e-mail vedoucího: vorobel@ipnp.troja.mff.cuni.cz

Abstrakt: Práce je zaměřena na hledání optimálního tvaru, materiálu a obalu scintilačního detektoru pro NEMO-3/SuperNEMO experiment. Pomocí Geant4 sotwaru a Monte Carlo simulační metody byly studovány čtyři konfigurace detektorů. Výsledkem každé konfigurace je statistický příspěvek do energetického rozlišení R. V první konfiguraci jedno- a dvojdimenzionální skeny ukázaly závislost hodnoty R na místě dopadu elektronického paprsku ve vstupní ploše. Spolehlivost simulací potvrzuje ve druhé konfiguraci získaná hodnota veličiny R (0.113), která se blíží naměřené hodnotě (0.115). Ve třetí a čtvrté konfiguraci byla provedena analýza materiálu (plastického a kapalného), obalu (zrcadlového a difúzního) a geometrického tvaru. Při geometrické analýze bylo využito výhodných optických vlastností Winstonova kuželu.
Na základě získaných údajů předkládá tato práce návrhy a obecná pravidla pro scintilační detektor, která mohou být využita při konstrukci kalorimetru SuperNEMO.
Klíčová slova: scintilátor, tvar, obal, Geant4, NEMO-3/SuperNEMO experiment.

Title: Detector for double beta decay investigation

Author: Aivaras Žukauskas

Department: Institute of Particle and Nuclear Physics

Supervisor: Ing. Vít Vorobel, Ph.D.

Supervisor's e-mail address: vorobel@ipnp.troja.mff.cuni.cz

Abstract: The aim of the diploma thesis is the search of the optimal shape, material and wrapping of the scintillation detector for NEMO-3/SuperNEMO experiment. Four different detector configurations have been studied by using Monte Carlo simulation method and Geant4 software toolkit. As a result, the statistical contribution to the energy resolution R was evaluated for different scintillator materials (plastic and liquid), shapes, specular and diffusive wrappings. In the first configuration one- and two-dimensional detector scans showed, how the value of R depends on the point where electron beam incidents detector's entrance face. In the second configuration, the simulated value of R (0.113) is in a good agreement with the experimental value (0.115), which signals the good reliability of simulations. In the third and fourth configurations the material/shape/wrapping analysis was performed. In geometrical shape analysis the advantageous optical properties of Winston cone have been used. The presented study provides general rules for scintillation detector, which may be applied in SuperNEMO calorimeter design.
Keywords: scintillator, shape, wrapping, Geant4, NEMO-3/SuperNEMO experiment

1 Introduction

Double beta decay is a very rare process with a long decay's half-time ($10^{17} - 10^{24}$ years). The research of this process can provide an information about the fundamental nature of neutrino. From the half-time of this decay it is possible to obtain the effective mass of neutrino.

NEMO-3 experiment, running since 1998, focuses on the double beta decay investigation [7]. It houses about 10 kg of radioactive double beta-decaying source. Its follower SuperNEMO experiment will extend this amount to 100 kg in the first phase.

SuperNEMO aims to enhance the global energy resolution from present 8% (FWHM at 3 MeV) in NEMO-3 to 4% in SuperNEMO and to reach the sensitivity of effective neutrino mass measuring less than 50 meV. For that purpose it is very important to improve the calorimeter's energy resolution.

The calorimeter of NEMO-3 is made from plastic scintillators. They provide a cheap and effective method of measuring energy of particles. SuperNEMO experiment will again use scintillators to provide energy measuring of the electrons and, perhaps, gamma particles[5]. The research is going in a wide spectrum of aspects. One of them, which tends to be the aim of this diploma thesis, is search of the optimal shape and wrapping of the scintillator.

The brief description of the double beta decay investigation and NEMO-3/SuperNEMO experiment is given in this diploma thesis. The mechanism of the scintillation process and light propagation is described too, because it is closely related to the aim of this work.

Monte Carlo simulations with a Geant4 software toolkit have been used to compare performances of several scintillator configurations of shapes, wrappings and materials. These configurations were proposed in NEMO-3/SuperNEMO collaboration for the purpose of Monte Carlo simulations' validation. The results will have an influence on the final calorimeter design. Several research groups in collaboration are working in this direction, thus, comparison between the individual results and/or measured data is (or will be in a near future) available. Comparison of the Monte Carlo results with the real measurements gives information about a reliability of the simulations

of other candidate configurations.

Four different detector configurations are presented. While three of them - UCL[1], CENBG[2] and ISM[3] - are the ones proposed in experiment's collaboration, the fourth one is the modified version of ISM configuration, where Winston cone is introduced (the idea is to use the advantageous optical properties of Winston cone [9]).

[1]University College London (UK)
[2]Centre d'Etudes Nuclèaires de Bordeaux Gradignan (France)
[3]Institute for Scintillation Material, Kharkov(Ukraine)

2 Double beta decay

In double beta decay two neutrons in the nucleus are converted to protons at the same time, and two electrons and two electron antineutrinos are emitted. This process is very rare in the nature, its half-time is $10^{18} - 10^{24}$ years (dependently on the isotope). It may be described in perturbation theory as the second order process.

This chapter discusses properties of neutrino in neutrinoless double beta decay and briefly describes properties of nuclei, where double beta decay may be observed.

2.1 Neutrinoless double beta decay

Double beta decay, observed in the nature, may be expressed following:

$$(Z, A) \rightarrow (Z + 2, A) + 2e^- + 2\bar{\nu}_e. \tag{2.1}$$

In the process (2.1), the total lepton number conservates ($\Delta L = 0$). We will mark this process as $2\nu\beta\beta$ decay. Its Feynman diagram is depicted in Figure 2.1(a). Emitted electrons have continuous energy spectrum, because we do not detect antineutrinos, which take away a certain part of energy.

There might exist the other process too, in which no neutrinos are emitted:

$$(Z, A) \rightarrow (Z + 2, A) + 2e^-. \tag{2.2}$$

The process (2.2) is much more interesting. Here only two electrons are emitted, and the conservation of total lepton number is violated ($\Delta L = 2$). Two neutrons in the

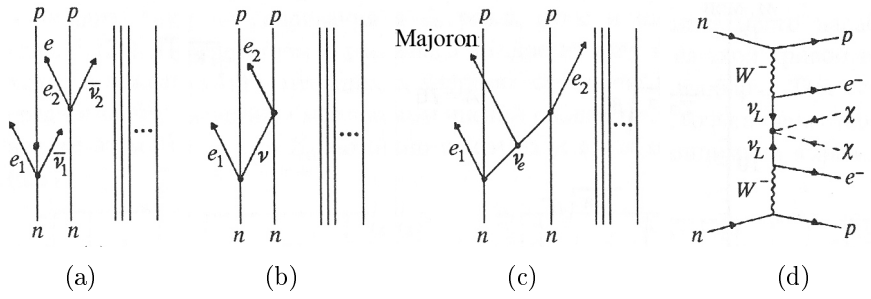

Figure 2.1: Feynman diagrams for $2\nu\beta\beta$ decay (a), $0\nu\beta\beta$ decay (b), one and two majoron decays $0\nu\chi\beta\beta$ (c) and $0\nu 2\chi\beta\beta$ (d).

same nucleus exchange virtual neutrino, as it is shown in Figure 2.1(b). This decay is called *neutrinoless* double beta decay. We will mark it as $0\nu\beta\beta$ decay.

Let us look into two following interactions:

$$n \to p + e^- + \bar{\nu}_e \tag{2.3a}$$

$$\nu_e + n \to p + e^- \tag{2.3b}$$

From the (2.3b) we see, that the neutron can absorb only ν_e, not $\bar{\nu}_e$. Thus, the neutrinoless double beta decay is allowed when the neutrino fulfills the folloving conditions:

- Neutrino must be Majorana particle. This means, that the neutrino and the antineutrino are identical, and that charge-conjugated neutrino equals to itself, i.e. $\nu = \nu^c$.
- Neutrino must have the rest mass, or there must exist the $(V+A)$ lepton current (Figure 2.2).

The second condition is necessary for the conservation of helicity (Figure 2.2). The right-handed (anti)neutrino emitted from the first vertex can be absorbed in the second vertex only when it flips its helicity, i.e. becomes left-handed. If the neutrino has the rest mass, helicity does not conserve, and this condition is fulfilled.

The effective neutrino mass can be extracted from the measured halftime of $0\nu\beta\beta$ decay [6]:

$$T_{1/2}^{-1} = |M_{0\nu\beta\beta}|^2 G_{0\nu\beta\beta} \langle m_{\beta\beta} \rangle^2 , \tag{2.4}$$

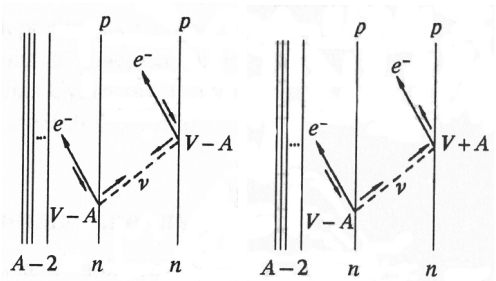

Figure 2.2: Diagrams for $0\nu\beta\beta$ decay in two-nucleon mechanism. Small arrows mark the helicity of particles.

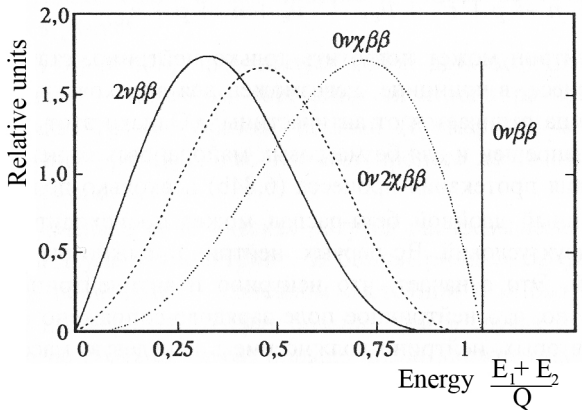

Figure 2.3: Full energy spectrum of both emitted electrons for different channels of double beta decay ($2\nu\beta\beta$, $0\nu\beta\beta$, $0\nu\chi\beta\beta$, $0\nu2\chi\beta\beta$).

where $M_{0\nu\beta\beta}$ is the nuclear matrix element, $G_{0\nu\beta\beta}$ is a known phase space factor that depends on the $Q_{\beta\beta}$ value. The half-life is proportional to the squared effective Majorana mass of neutrino, $\langle m_{\beta\beta}\rangle^2$, which is given by a sum over the masses m_i of the mass eigenstates, $\langle m_{\beta\beta}\rangle = \Sigma_{i=1,2,3} U_{ei}^2 m_i$, weighted by the squared elements, U_{ei}^2 of the PMNS neutrino mixing matrix.

In $0\nu\beta\beta$ process no neutrinos are emitted. The total kinetic energy of both electrons $E_{\beta_1} + E_{\beta_2}$ is equal to the mass difference between parent and daughter nuclei, i.e. $E_{\beta_1} + E_{\beta_2} = Q_{\beta\beta}$. In the kinetic energy spectrum the energy of $0\nu\beta\beta$ process is represented as a line (Figure 2.3) at the value $Q_{\beta\beta}$.

The kinetic energy of $2\nu\beta\beta$ process $E_{\beta_1} + E_{\beta_2}$ will have a continuous spectrum.

In the literature one may find also the other possible modes of double beta decay, for example, neutrinoless double beta decay with one or two hypothetical massless majorons (χ) emitted:

$$(Z, A) \rightarrow (Z + 2, A) + 2e^- + \chi, \tag{2.5}$$

$$(Z, A) \rightarrow (Z + 2, A) + 2e^- + \chi + \chi. \tag{2.6}$$

In order to investigate double beta decay, one must carefully select appropriate radioactive isotopes. A lot of unstable nuclei are inapplicable for the research because of huge single beta decay background. In the next subchapter we shall discuss properties of double beta decaying nuclei which makes the process observable. The selection rules for the "good" isotopes shall be considered in the chapter 3.

2.2 Double beta decaying nuclei

The stability of nucleus, in respect to the weak decay process, may be described by its atomic mass $m(Z, A)$. A good approximation of dependency of the atomic mass m on the proton number Z and the nucleon number A is expressed by the semi-empirical Weizsäcker mass formula [10]:

$$m(Z,A) = Zm_{\mathrm{H}} + (A-Z)m_n - a_{\mathrm{V}}A + a_{\mathrm{S}}A^{2/3} + a_{\mathrm{C}}Z^2A^{-1/3} + a_{\mathrm{A}}\frac{(2Z-A)^2}{A} + \delta_{\mathrm{P}}, \quad (2.7)$$

where m_{H} is the mass of hydrogen, m_n is the mass of neutron, a_{V}, a_{S}, a_{C} and a_{A} are according constants for volume, surface, Coulomb and asymmetry energy terms in the formula.

In (2.7), we focus on the so-called *pairing* term, δ_{P}. Nucleus is more stable when it has an even number of protons and/or neutrons. This phenomenon implies three δ_{P} values:

$$\delta_{\mathrm{P}} = \begin{cases} -a_{\mathrm{P}}A^{-1/2} & \text{for even-even nuclei (even } A\text{),} \\ 0 & \text{for even-odd and odd-even nuclei (odd } A\text{),} \\ +a_{\mathrm{P}}A^{-1/2} & \text{for odd-odd nuclei (even } A\text{),} \end{cases} \quad (2.8)$$

where $a_{\mathrm{P}} \approx 12$ MeV.

Formula (2.7) expresses the quadratic dependency of the atomic mass $m(Z, A)$ on the

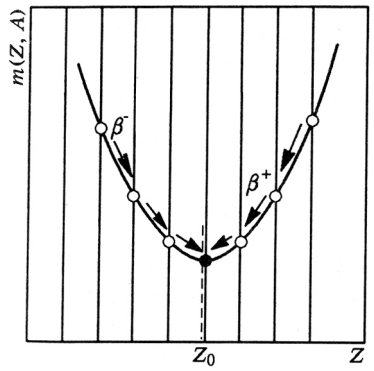

(a) Parabola of nuclei with odd A

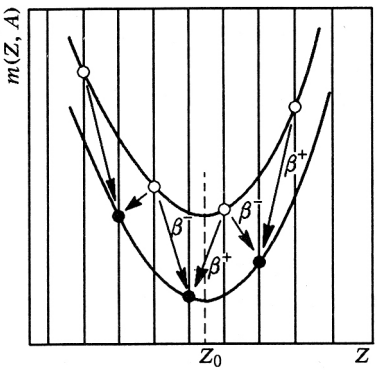

(b) Parabolas of nuclei with even A

Figure 2.4: Dependency of the atomic mass $m(Z, A)$ on Z when A is fixed. Positions of stable nuclei are marked as black circles on the parabola, positions of unstable nuclei are white (empty) circles. Z_0 marks the minimum of parabola.

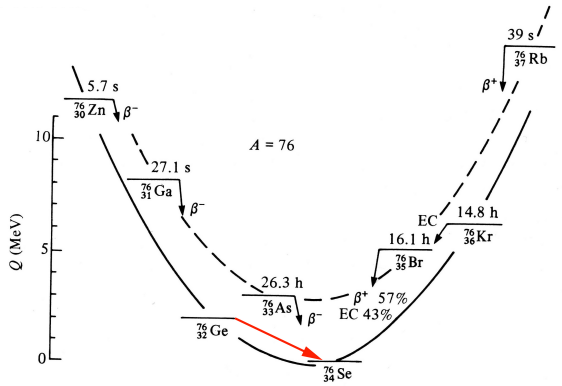

Figure 2.5: Spectrum of atomic mass for isobars with $A = 76$.

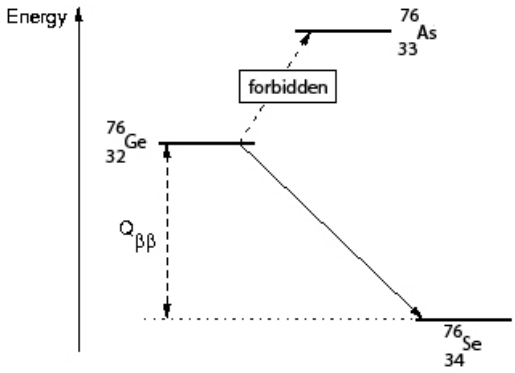

Figure 2.6: Energy scheme of the double beta decay from $^{76}_{32}$Ge to $^{76}_{34}$Se.

proton number Z:

$$m(Z, A) \sim const + \alpha Z + \beta Z^2 + \delta_{\mathrm{P}}. \tag{2.9}$$

In order to depict this dependency we must take into account values of δ_{P}. For $\delta_{\mathrm{P}} = 0$ (odd A) we get one parabola, as shown in Figure 2.4(a). Nuclei lying on this parabola transits via β decay to the next lower position until they reach the stable state with the lowest energy, marked as Z_0.

For nuclei with even A there are two parabolas 2.4(b): the upper one for odd-odd nuclei, and the lower one for even-even nuclei. Parabolas are separated by $2\delta_{\mathrm{P}}$, as follows from (2.8). In this case, nuclei transit from one parabola to the other and always end up on the lower one, because there cannot be (with a few exceptions) stable odd-odd nuclei.

Let us take a closer look to the nuclei with even A. We may use isobars with $A = 76$ as a concrete example. Figure 2.5 shows their allocation on the parabolas and possible

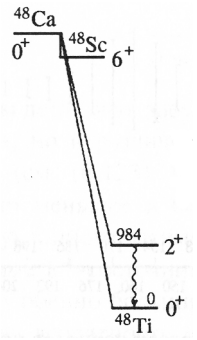

Figure 2.7: $\beta\beta$ decay of ^{48}Ca.

β decays. We can see there, that nuclei overpass the unstable states and end up as $^{76}_{32}$Ge or $^{76}_{34}$Se. $^{76}_{32}$Ge cannot decay via β decay into the $^{76}_{33}$As, because $^{76}_{33}$As has a higher energy than $^{76}_{32}$Ge (Fig. 2.6). However, $^{76}_{32}$Ge may change its nuclear charge Z by two units and decay into the $^{76}_{34}$Se, as it is depicted in Figure 2.5 by the red arrow. This kind of decay is double beta decay.

Figures 2.5 and 2.6 imply that all double beta decay candidates must satisfy following conditions: They are even-even nuclei, which, thanks to the pairing energy, lie in lower positions in comparing to their odd-odd neighbors. Thus, they cannot decay via β^+ or β^- decay. One of rare exceptions is ^{48}Ca, which could decay into the lower lying isobar ^{48}Sc (Figure 2.7), but this transfer is forbidden because of big spin differences ($0^+ \rightarrow 6^+$).

Only a few $\beta\beta$ emitting isotopes fulfill such conditions. The most experimentally observed are ^{76}Ge, ^{82}Se, ^{48}Ca, ^{96}Zr, ^{100}Mo, ^{136}Xe, ^{150}Nd.

There are also other double beta decay processes possible: double positron decay, double electron capture and already mentioned neutrinoless decay with the emission of one or two Majorons. They have never been observed experimentally.

3 Experiment NEMO-3/SuperNEMO

The Neutrino Ettore Majorana Observatory (NEMO-3/SuperNEMO) is a double beta decay experiment. The philosophy behind NEMO is the direct detection of the two electrons from double decay by a tracking device and a calorimeter. Here we will describe only the calorimeter of NEMO-3 detector in more details (chapter 3.2), because it is closely related with the aim of this diploma thesis. One can find a comprehensive description of whole NEMO-3 experiment in [7].

3.1 The NEMO-3 Experiment

The NEMO-3 detector is now installed in LSM - Laboratoire Souterrain de Modane[1] in France, at a depth of 4800 m water equivalent. It is divided into 20 identical sectors which form a cylindrical shape, 3.1m in diameter and 2.5m in height (Figure 3.1). The sectors each contain foils covered with chosen double beta decay isotopes. The source foils are fixed vertically between two concentric cylindrical tracking volumes composed of 6180 open octagonal drift cells. Each cell consists of central anode wire

[1] also known as Fréjus Underground Laboratory

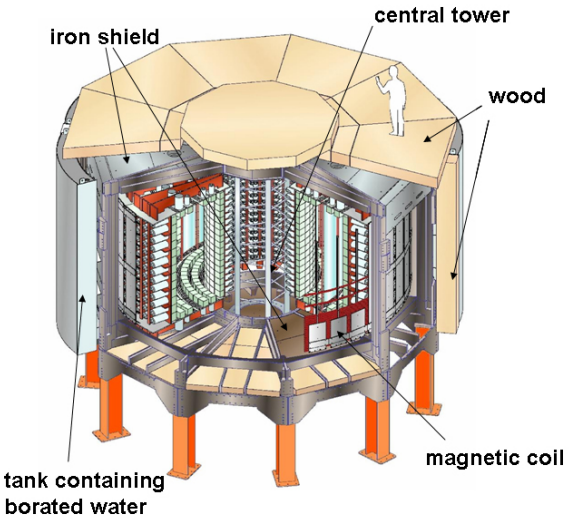

Figure 3.1: An exploded view of the NEMO-3 detector. Note the coil and various shields for stopping external background. The parafin shield under the central tower is not shown on the picture.

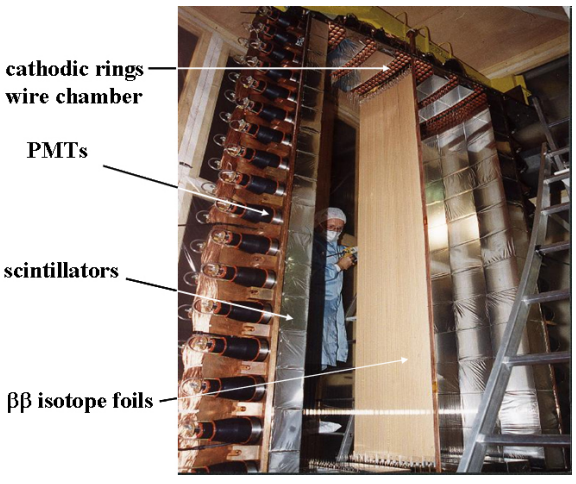

Figure 3.2: View of one sector in the source mounting room.

surrounded by 8 cathode wires. The drift cells are 270 cm long, operating in Geiger mode at 7mbar above atmospheric pressure and use a gas mixture of helium (99%), argon (1%), ethyl alcohol (40 mbar % partial pressure) and water (1500 ppm). The cells run vertically and three-dimensional tracking is accomplished with the arrival time of the signals on the anode wires and the plasma propagation times to the cathodic rings at the ends of the drift cells.

A solenoid surrounding the detector produces a 25G magnetic field parallel to the foil axis, in order to identify the particle charge (distinguish e^+ from e^-).

Energy and time-of-flight measurements are acquired from plastic scintillators covering the two vertical surfaces of the active tracking volume. To further enhance the acceptance efficiency, the end-caps (the top and bottom of the detector) are also equipped with scintillators in the spaces between the drift cell layers. Figure 3.2 shows a picture of one sector of the NEMO-3 detector.

Typical double beta decay event in NEMO-3 detector is shown in Figure 3.3. The red lines marks trajectories of the particles, the circles radii correspond to the transverse distance from the anode wire for each fired cell, they are not error bars. At the end of each trajectory hited scintillators are shown.

An external shield, in the form of 20 cm of low radioactivity iron, covers the detector

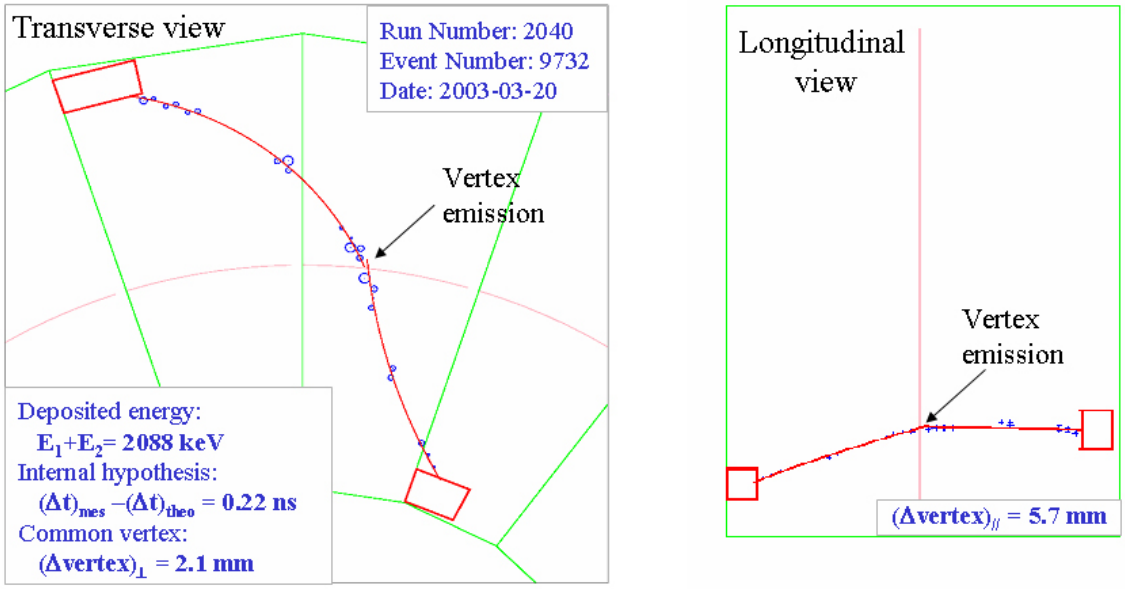

Figure 3.3: Double beta event observed from ^{100}Mo.

to reduce gamma rays and thermal neutrons. Outside of this iron there is a borated water shield to thermalize fast neutrons and capture thermal neutrons.

In the NEMO-3 detector, electrons, positrons, photons and alpha particles can be identified. Thus, the detector is able to detect multi-particle events in the low energy domain of natural radioactivity.

The primary design feature of the NEMO-3 experiment was to have the detector and the source of the double beta decay independent, unlike the case of the ^{76}Ge experiments. This permits one to study several double beta decay isotopes, a critical point is to be able to confirm an excess of $0\nu\beta\beta$ events from one isotope with another isotope.

The choice of which nuclei to study (Figure 3.4) was affected by several parameters. These include the transition energy ($Q_{\beta\beta}$), the nuclear matrix elements ($M_{0\nu\beta\beta}$ and $M_{2\nu\beta\beta}$) of the transitions for $0\nu\beta\beta$ and $2\nu\beta\beta$ decays, the background in the energy region surrounding the $Q_{\beta\beta}$ value, the possibility of reducing the radioactivity of the isotope studied to acceptable levels, and finally the natural isotopic abundance of the candidate. Typically only isotopic abundances greater than 2% were considered. A good criterion for isotope selection is the $Q_{\beta\beta}$ value with respect to backgrounds ($Q_{\beta\beta} > 2.6$ MeV).

Five nuclei satisfy these two criteria: ^{116}Cd ,^{82}Se, ^{100}Mo, ^{96}Zr and ^{150}Nd (with respective $Q_{\beta\beta}$ values of 2804.7, 2995.2, 3034.8, 3350.0 and 3367.1 keV and respective

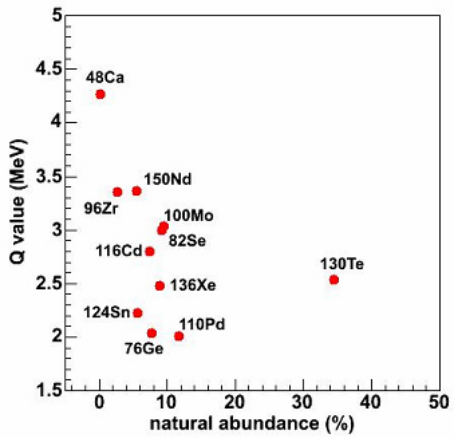

Figure 3.4: Natural abundance and transition energy $Q_{\beta\beta}$ of double beta decaying isotopes

isotope abundance values of 7.5%, 9.2%, 9.6%, 2.8% and 5.6%). Given this list and the availability of ^{100}Mo, much effort has been focused by the NEMO collaboration on this isotope. However the focus is not exclusively on ^{100}Mo, in view of the fact that the detector can house several different sources.

Besides the five mentioned isotopes, additional double beta decay sources are included: ^{48}Ca because of its impressive $Q_{\beta\beta}$ value ($Q_{\beta\beta} = 4272.0$keV), Te has a high abundance (33.8%), and Cu serves for external background measurement.

The isotopes, which are studied in NEMO-3, are brought together in Table 1. Their distribution in 20 sectors of detector is depicted in Figure 3.5.

Table 1: Isotopes used in NEMO-3

	^{100}Mo	^{82}Se	^{116}Cd	^{96}Zr	^{150}Nd	^{48}Ca	^{130}Te	$^{\text{nat}}$Te	Cu
Mass, g	6914	932	405	9.4	37.0	7.0	454	491	621
$Q_{\beta\beta}$, keV	3034	2995	2805	3350	3367	4772	2529		

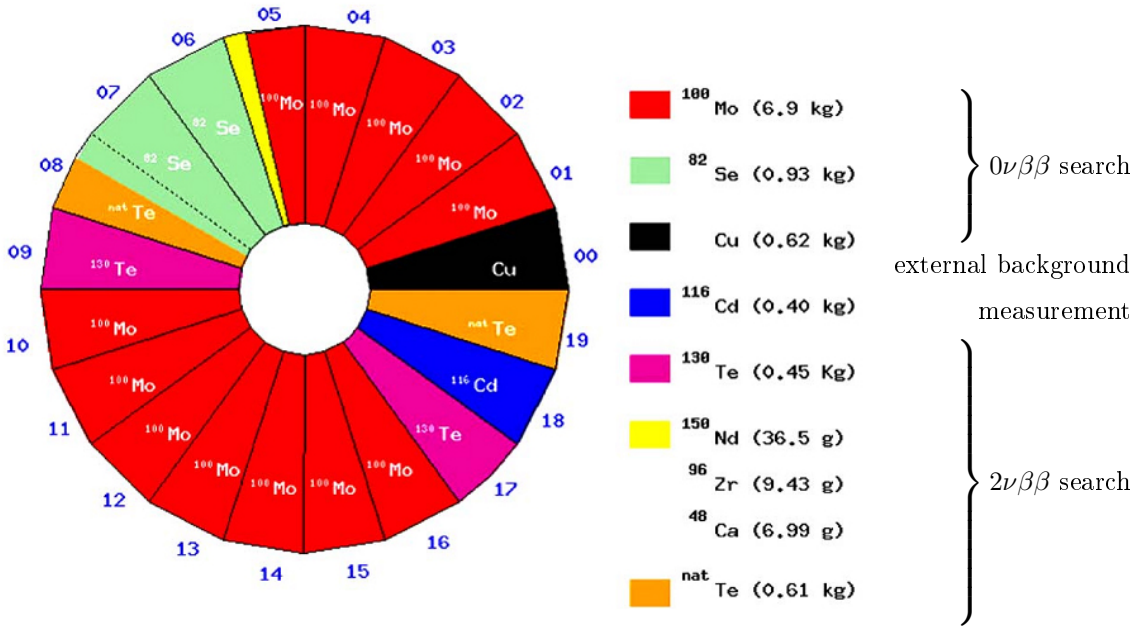

Figure 3.5: The source distribution in the 20 sectors of NEMO-3.

3.2 Design of the calorimeter

The calorimeter is constructed with 1940 counters, each of which is made with a plastic scintillator, lightguide and low radiation PMT (3" or 5"). The gains of the PMTs have been adjusted to cover energies up to 12 MeV. The plastic scintillators were chosen to minimize backscattering and for their radiopurity. The scintillators completely cover the two cylindrical walls which surround the tracking volume.

The chemical nature of the material using for scintillator production is the solid solution of a scintillating agent p-Terphenyl (PTP) and a wavelength shifter 1.4-di-(5-phenyl-2-oxazoly)benzene (POPOP) in polystyrene. The mass fractions of polystyrene, PTP and POPOP were chosen. These are, respectively, 98.75%, 1.2% and 0.05% for the end-caps scintillators and 98.49%, 1.5% and 0.01% for the blocks of the walls.

There are seven types of scintillator which are distinguished by their different shapes which have been designed to fit the circular geometry of the NEMO-3 detector. All the scintillator blocks have a thickness of 10 cm which is a compromise to obtain a high enough efficiency (50% at 500 keV) for γ-ray tagging with plastic scintillators without loss of transparency of the scintillation light for the electron energy resolution. The γ-ray tagging allows the measurement of the residual radioactivity of the source foil as well as rejecting background events.

The energy resolution (FWHM) of the calorimeter is 14% at 1 MeV for the scintillators equipped with the 5" PMTs on the external wall and 17% for the 3" PMTs on the internal wall [3].

3.3 Sensitivity and preliminary results of NEMO-3

The NEMO 3 detector has been running reliably since February 2003. The $2\nu\beta\beta$ decay has been measured for ^{82}Se and ^{100}Mo with very high statistics and better precision than the previous measurements. All components of the background in the $0\nu\beta\beta$ energy window have been measured directly using different analysis channels in the data. The limits at the 90% C.L. are:

- Limit on the $0\nu\beta\beta$ half-time:
  $T_{1/2}(0\nu\beta\beta) > 5.8 \times 10^{23}$ yr for ^{100}Mo and 2.1×10^{23} yr for ^{82}Se,

- Limit on the Majorana neutrino effective mass: $\langle m_\nu \rangle < 0.4 - 0.7$ eV for ^{100}Mo, $\langle m_\nu \rangle < 1.4 - 2.2$ eV for ^{82}Se.

Exposition time for ^{100}Mo and ^{82}Se is 693 days.

3.4 SuperNEMO: objectives

The NEMO collaboration in association with new UK, US, Russian and Japanese groups started in December 2003 studying the feasibility of an extrapolation of the NEMO 3 technique to a detector with a mass of at least 100 kg of enriched $\beta\beta$ isotope in order to reach a sensitivity of 50 meV on the effective neutrino mass.

The SuperNEMO detector would use the NEMO-3 technical choices: a thin source between two tracking volumes surrounded by a calorimeter. The main features to improve compare to NEMO-3 are the energy resolution, the $0\nu\beta\beta$ detection efficiency, the source radiopurity and the background rejection.

SuperNEMO detector would be composed of several identical modules (for example 20 modules with 5 kg of radioactive source). Such modular design allows to begin the data collection before the end of the last module construction and mounting. Each module would consist of one source foil, one tracking volume and one calorimeter, these three parts being independent to make easier the construction, mounting and eventual changes. The detector will be plane and not cylindrical as NEMO-3 was.

The $2\nu\beta\beta$ decay contribution to $0\nu\beta\beta$ backgrounds is related directly to its half-time and to the detector energy resolution. The global resolution, which had to be better than 8% (FWHM) at 3 MeV to strongly reduce the $2\nu\beta\beta$ decay contribution, depends on the calorimeter resolution and energy losses in both source foils and tracking volume.

The SuperNEMO calorimeter part will use plastic or organic liquid scintillators coupled to PMTs or photodiodes. Use of silicon detectors is excluded because of the large backscattering of electrons. The goal is to reach a calorimeter resolution better than 4% (FWHM) at 3 MeV.

There are two options for the thickness of the scintillator blocks in the SuperNEMO calorimeter: to use a small one (2 cm) or a large one (10-20 cm). In the first case,

the light collection should be better but only for electrons and the addition of a gamma calorimeter (in plastic or liquid scintillators) surrounding the detector should be necessary. Using the 10-20 cm option there is a risk to lose scintillation light.

The aim of this diploma thesis, as it is already mentioned in introduction, is to optimize the shape and the wrapping of the scintillator so that the light collection would be the most efficient. Thus, going further, the next steps would be the understanding of the process of scintillation, Monte Carlo simulations, and their verification by measurements or other independent simulations.

4 Scintillation detectors in nuclear and particle physics

The scintillation detector is undoubtedly one of the most often and widely used particle detection devices in nuclear and particle physics today. It makes use of the fact that certain materials when struck by a nuclear particle or radiation, emit a small flash of light, i.e. a scintillation. When coupled to an amplifying device such as a photomultiplier, these scintillations can be converted into electrical pulses which can then be analyzed and counted electronically to give information concerning the incident radiation.

4.1 General characteristics

In general, the scintillator signal is capable of providing a variety of information. Among its most outstanding features are [4]:

- Sensitivity to energy. Above a certain minimum energy, most scintillators behave in a near linear fashion with respect to the energy deposit. Since the photomultiplier is also a linear device (when operated properly), the amplitude of the signal will also be proportional to the deposited energy.
- Fast time response. Scintillation detectors are fast instruments in the sense that their response and recovery times are short relative to other types of detectors. Thus it allows timing information, fast recovery time also allows scintillation detectors to accept higher count rates since the dead time is reduced.
- Pulse shape discrimination. With certain scintillators, it is possible to distinguish between different types of particles by analyzing the shape of the emitted light pulses.

Scintillator materials exhibit the property known as *luminescence*. Luminescent materials, when exposed to certain forms of energy, for example, light, heat, radiation, etc., absorb and reemit the energy in the form of visible light. If the reemision occurs immediately after absorption or more precisely within 10^{-8} s (10^{-8} being roughly the time taken for atomic transitions), the process is usually called *fluorescence*. However, if reemision is delayed because the excited state is metastable, the process is

called *phosphorescence* or *afterglow*. In such cases, the delay time between absorption and reemision may last anywhere from a few microseconds to hours depending on the material.

While many scintillating materials exist, not all are suitable as detectors. In general, a good detector scintillator should satisfy the following requirements:

- high efficiency for conversion of exciting energy to fluorescent radiation;
- transparency to its fluorescent radiation so as to allow transmission of the light;
- emission in a spectral range consistent with the spectral response of existing photomultipliers;
- a short decay constant, τ.

At present, six types of scintillator materials are in use: organic crystals, organic liquid and plastic scintillators, inorganic crystals, gases and glasses. In the following sections we will briefly describe organic plastic and liquid scintillators, because they take priority in the SuperNEMO experiment.

4.2 Organic scintillators

The organic scintillators are aromatic hydrocarbon compounds containing linked or condensed benzene-ring structures. Their most distinguished feature is a very rapid decay time on the order of a few nanoseconds or less.

Scintillation light in these compounds arises from transitions made by the free valence electrons of the molecules. These delocalized electrons are not associated with any particular atom in the molecule and occupy what are known as the *π-molecular orbitals*. A typical energy diagram of these orbitals is shown in Figure 4.1, where there are distinguished the spin singlet states from the spin triplet states. The ground state is a singlet state, denoted by S_0. Above this level are the excited singlet states ($S^*, S^{**}, \ldots$) and the lowest triplet state (T_0) and its excited levels ($T^*, T^{**}, \ldots$). Also associated with each electron level is a fine structure which corresponds to excited vibrational modes of the molecule. The energy spacing between electron levels

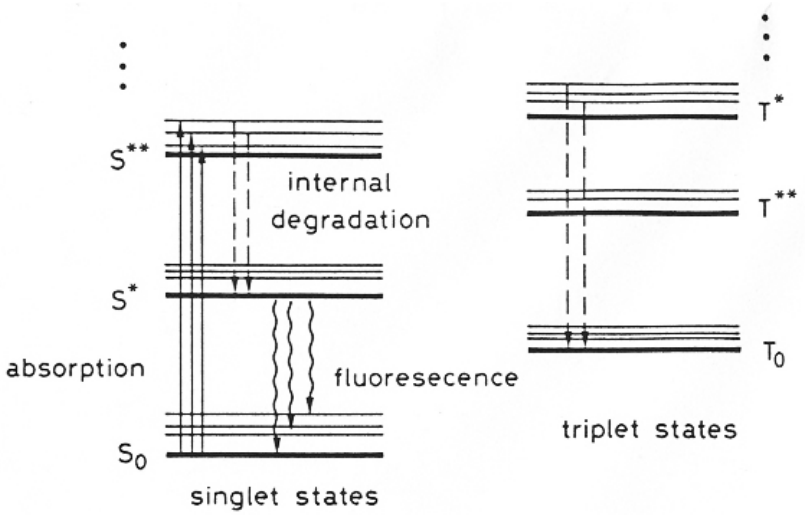

Figure 4.1: Energy level diagram of an organic scintillator molecule. For clarity, the singlet states (denoted by S) are separated from the triplet states (denoted by T).

is on the order of a few eV whereas that between vibrational levels is of the order of a few tenths of eV. Ionization energy from penetrating radiation excites both the electron and vibrational levels as shown by the solid arrows. The singlet excitations generally decay immediately ($\leq$ 10 ps) to the S^* state without the emission of radiation, a process which is known as *internal degradation*. From S^*, there is generally a high probability of making a radiative decay to one of the vibrational states of the ground state S_0 (wavy lines) within a few nanoseconds time. This is the normal process of fluorescence which is described by the prompt exponential decay. The fact that S^* decays to excited vibrational states of S_0, with emission of radiation energy less than that required for the transition $S_0 \rightarrow S^*$ also explains the transparency of the scintillators to their own radiation.

For the triplet excited states, a similar internal degradation process occurs which brings the system to the lowest triplet state. There is also a possibility for the T_0 state to decay by interacting with another excited T_0 molecule,

$$T_0 + T_0 \rightarrow S^* + \text{phonons} \tag{4.1}$$

to leave one of the molecules in the S^* state. Radiation is then emitted by the S^* as described above. This light comes after a delay time characteristic of the interaction between the excited molecule and is the delayed or slow component of scintillator light. The contribution of this slow component to the total light output is only

significant in certain organic materials, however.

Because of the molecular nature of luminescence in these materials, organics can be used in many physical forms without the loss of their scintillating properties. As detectors, they have been used in the form of pure crystals and as mixtures of one or more compounds in liquid and solid solutions.

4.3 Energy resolution

For detectors which are designed to measure the energy of incident radiation, the most important factor is the energy resolution. In general, the resolution can be measured by sendind a monoenergetic beam of radiation into the detector and observing the result. Ideally, one would like to see a sharp delta-function peak. In reality, this is never the case and one observes a peak structure with a finite width, usually Gaussian in shape. This width arises because of fluctuations in the number of ionizations and excitations produced.

The resolution is usually given in terms of the *full width at half maximum* of the peak (FWHM). Energies which are closer than this interval are usually considered unresolvable. If we denote this width as ΔE, then the relative resolution at the energy E is

$$\text{Resolution} = \frac{\Delta E}{E}. \tag{4.2}$$

In addition to the fluctuations in ionization, a number of external factors can affect the overall resolution of a detector. This includes effects from the associated electronics such as noise, drifts, etc. Assuming all these sources are independent and distributed as Gaussians, the total resolution E is then given by

$$(\Delta E)^2 = (\Delta E_{det})^2 + (\Delta E_{noise})^2 + (\Delta E_{drift})^2 + \ldots. \tag{4.3}$$

The performance of each configuration discussed in this thesis will be presented as the statistical contribution to the energy resolution:

$$R = \frac{\Delta E_{det}}{E}, \tag{4.4}$$

which depends on the mean number of signal produced events N:

$$R = 2.35\frac{\sqrt{FN}}{N}, \tag{4.5}$$

where the factor 2.35 relates the standard deviation of a Gaussian to its FWHM, F is the Fano factor. For scintillators, $F = 1$, and N is the number of produced photoelectrons. Thus, we get

$$R = \frac{2.35}{\sqrt{N}}. \tag{4.6}$$

The statistical contribution to the energy resolution is chosen because of several reasons. It is easily comparable quantity, and, in addition, the geometry, material and the wrapping of the detector also has an influence on it.

5 Optical photon simulations

5.1 Optics in Geant4

Geant4 is a body of C++ code that models and simulates using Monte Carlo method the interaction of particles with matter [2]. The code is distributed freely under an open software license. Geant4 propagates particles - elementary particles and ions, both stable and unstable - through any geometrical arrangement of material. It is a simulation tool used in this diploma thesis to investigate various detectors' performances. Its physics processes for optical photons are shortly described here.

A photon [1] is considered to be optical when its wavelength is much greater than the typical atomic spacing, for instance when $\lambda \geq 10$ nm. The status of the photon is defined by two vectors, the photon momentum ($\vec{p} = \hbar\vec{k}$) and photon polarization ($\vec{e}$). In Geant4 optical photons are treated as a class of particle distinct from their higher energy gamma cousins. This implementation allows the wave-like properties of electromagnetic radiation to be incorporated into the optical photon process.

Production of an optical photon in a detector is primarily due to Cerenkov effect or scintillation.

Optical photon interactions

Optical photons undergo three kinds of interactions: elastic (Rayleigh) scattering, absorption and medium boundary interactions.

Rayleigh scattering is usually unimportant. For $\lambda = 0.2\mu m$ we have $\sigma_{Rayleigh} \approx 0.2b$ for N_2 or O_2, which mean a free path at $\approx$ 1.7km in air and $\approx$ 1m in quartz.

Absorption is important for optical photons. It determines the lower λ limit in the window of transparency of the radiator. Absorption competes with photo-ionization in producing the signal in the detector, so it must be treated properly in the tracking of optical photons.

Medium boundary effects are three, depending on the nature of the two materials joining at that boundary:

- Case dielectric-dielectric: The photon can be transmitted or reflected. In case where the photon can only be reflected, total internal reflection takes place.

The behaviour of a photon at the surface boundary is determined by three quantities:

1. refraction or reflection angle, this represents the kinematics of the effect;
2. amplitude of the reflected and refracted waves, this is the dynamics of the effect;
3. probability of the photon to be refracted or reflected, this is the quantum mechanical effect which we have to take into account if we want to describe the photon as a particle and not as a wave.

- Case dielectric-metal: The photon can be absorbed by the metal or reflected back into the dielectric. If the photon is absorbed it can be detected according to the photoelectron efficiency of the metal.
- Case dielectric-black material: A black material is a tracking medium for which the user has not defined any optical property. In this case the photon is immediately absorbed undetected.

Scintillation

The generation of scintillation light can be simulated by sampling the number of photons from a Poisson distribution. This distribution is based on the energy lost during a step in a material and on the scintillation properties of that material. The frequency of each photon is sampled from the empirical spectra. The photons are generated evenly along the track segment and are emitted isotropically into 4π with a random linear polarization.

Wavelength shifting

Wavelength shifting (WLS) materials are used in many high-energy particle physics experiments. They absorb light at one wavelength and re-emit light at a different wavelength and are used for several reasons. For one, they tend to decrease the self-absorption of the detector so that as much light reaches the PMTs as possible. WLS material is used in NEMO-3 scintillators, thus, it must be properly included in simulations too.

A WLS material is characterized by its photon absorption and photon emission spectrum and by a possible time delay between the absorption and re-emission of the photon. Wavelength shifting may be simulated by specifying these empirical parameters for each WLS material in the simulation. It is sufficient to specify:

- A relative spectral distribution as a function of photon energy for the WLS material.
- The absorption length of the material as a function of the photon's momentum.
- The relative emission spectrum of the material as a function of the photon's momentum.
- The WLS time constant, accounting any time delay which may occur between absorption and re-emission of the photon.

6 Studied configurations

Optical photon simulations take an important place in the research and developement of SuperNEMO. The choice of final scintillators' shape and wrapping will be based on Monte Carlo simulations. Several laboratories (UCL[1], CENBG[2], ISM[3], JINR[4]) proposed their testing configurations of scintillators with certain shapes, materials and wrappings. These scintillators has to be manufactured and tested during R&D of SuperNEMO experiment. Simulation group - CENBG, ISM, Prague[5] and Austin[6] - recently are in charge to simulate performances of those configurations for several reasons:

- comparison between individual simulation groups will give so-called "relative" verification. The same or similar result from independent simulations would be the proof of good knowledge of simulation.
- comparison of simulation results with measured data wil give "absolute" verification. This will prove the reliability of simulations, on which we could base the following research.

In the next chapters we will discuss and represent results of four configurations: UCL, CENBG, ISM and modified ISM, where Winston cone's shape is used instead of original conical part. JINR configuration differs in many aspects from the ones proposed by other laboratories, it will not be considered in this work.

6.1 UCL configuration

UCL has proposed a configuration of plastic scintillator connected with a flat EMI D724KFL PMT. The detector is wrapped in a special Vikuiti specular foil [8], as it is shown in Figure 6.1 (Figure 6.2 shows the detector in Geant4 visualization environment). Detector's dimensions are 50x50x20 mm, the thickness of Vikuiti wrapping is 64 micron.

[1]University College London (UK)
[2]Centre d'Etudes Nuclèaires de Bordeaux Gradignan (France)
[3]Institute for Scintillation Material, Kharkov(Ukraine)
[4]Joint Instititute for Nuclear Research, Dubna (Russia)
[5]Vit Vorobel and Aivaras Zukauskas, Charles University
[6]University of Texas at Austin

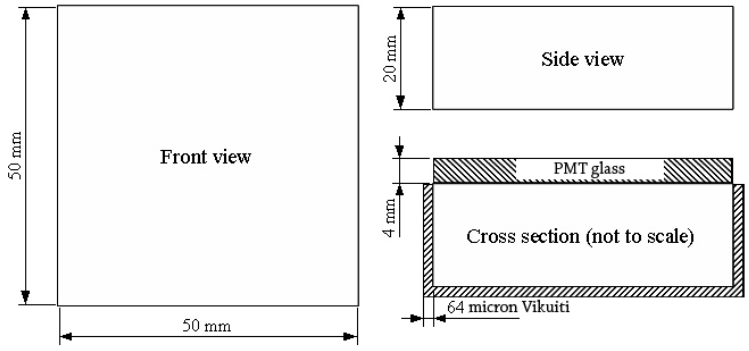

Figure 6.1: Geometry, measurements and cross-section of the UCL scintillator.

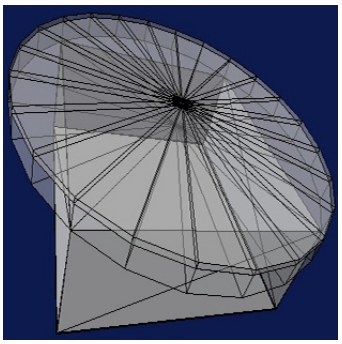

Figure 6.2: UCL detector in Geant4 visualisation environment.

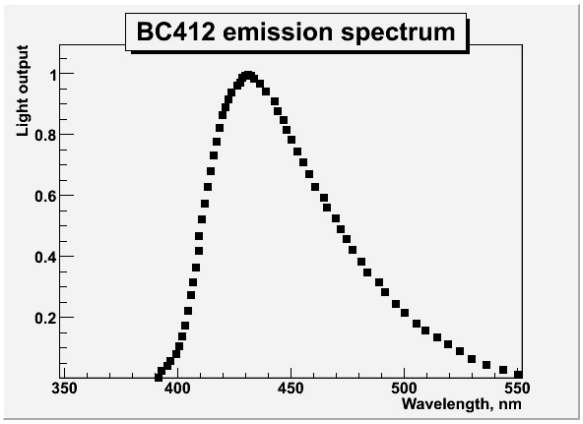

Figure 6.3: Emission spectrum of UCL detector.

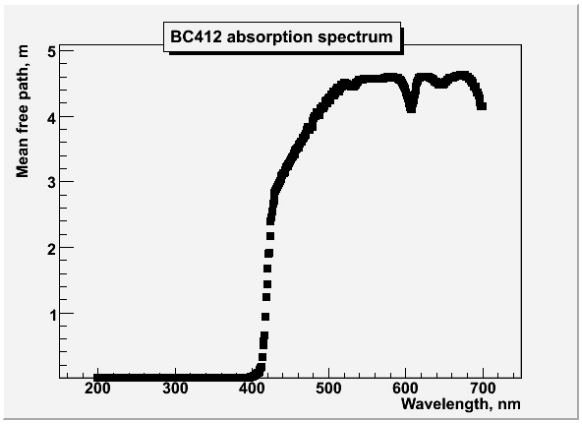

Figure 6.4: Absorption spectrum of UCL detector.

The base of the scintillator material is polyvinyltoluene. Other material properties used in the simulation are written in Table 2. The manufacturer (Saint Gobain company) provides scintillator emission spectrum, which is shown in Figure 6.3. The absorption spectrum of the scintillator had to be constructed from the absorption spectra of its constituents (p-Terphenyl, polystyrene and POPOP) and is shown in Figure 6.4. Vikuiti reflection coefficient depends on the wavelength of reflected photon; it is shown in Figure 6.5. The maximal quantum efficiency of the PMT is 25 % at 400 nm wavelength (Figure 6.6).

In order to get the value of the statistical contribution to the energy resolution R, we shoot a 1000 primary electrons with 1 MeV kinetic energy each in the centre of the scintillator. Each such electron generates about 10000 optical photons. The actual number fluctuates according to normal distribution within the interval $\pm\sqrt{N_p}$, where

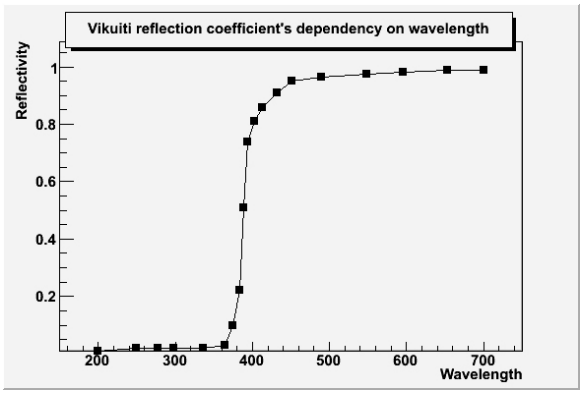

Figure 6.5: Dependency of Vikuiti's specular wrapping reflectivity on the wavelength.

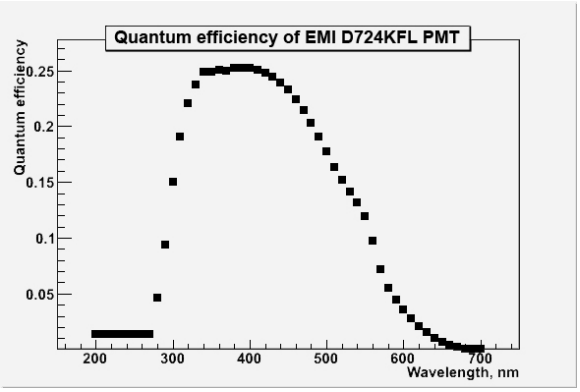

Figure 6.6: Dependency of PMT's quantum efficiency on the wavelength.

Table 2: UCL scintillator's material properties

Property	Value
Density	1.032 g/cc
Refractive index	1.58
Light Output, % Anthracene	60
Light Output, photons/MeV	10000
Wavelength of max. emission	434 nm
Mean free path	250 cm

N_p is the number of primary electrons, i.e. 10000 in this case. The averaged value of events registered in the PMT gives us the number of produced photoelectrons N. Then, using (4.6), we can count the statistical contribution to energy resolution R.

It is logical to consider the fact, that the value of R will be different if we shoot the

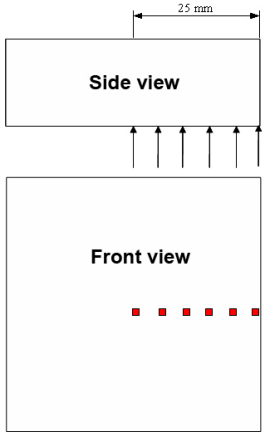

Figure 6.7: Scheme of investigation of R dependency on the entrance of the incident electrons.

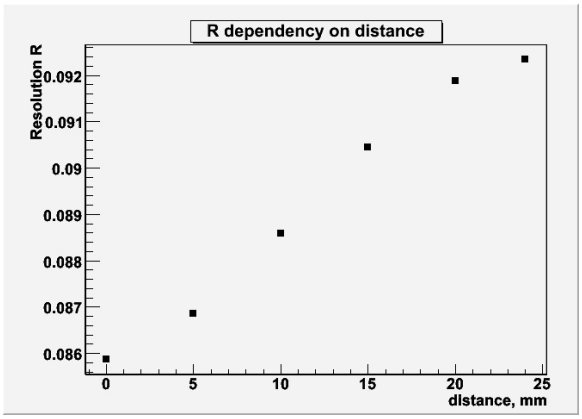

Figure 6.8: R dependency on the entrance of the incident electrons.

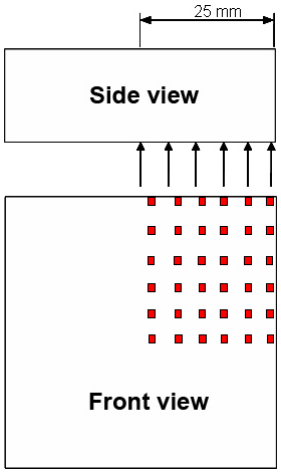

Figure 6.9: Scheme of the two-dimensional scan of the UCL scintillator.

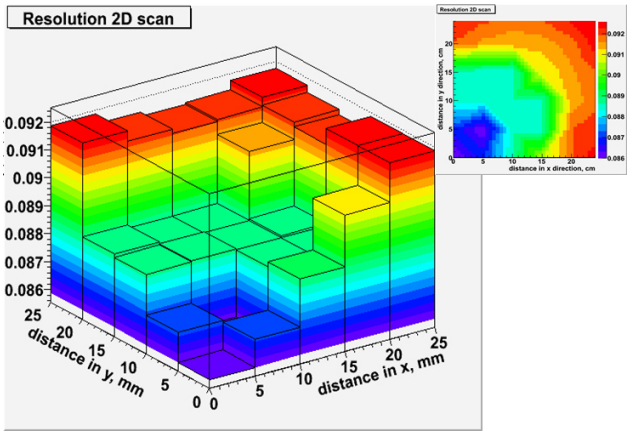

Figure 6.10: Result of the two-dimensional scan. Energy resolution R is plotted on the Z axis.

electron elswhere, not in the centre of the scintillator. To study this phenomenon, we have chosen six shooting points starting at the centre and gradually approaching the edge with a 5 mm step, as it is depicted in Figure 6.7. The eventual dependency of R is plotted in the Figure 6.8. We can see, that approaching the edge of the scintillator, the value of R rises from 0.086 to 0.092.

In a similar fashion we made a full two-dimensional scan of the scintillator. Due the symmetry of the scintillator, scanning only the quarter is sufficient (Figure 6.9). The result is shown in Figure 6.10. Going farther from the center in any direction, the value of R rises, while at the edges of the detector it remains nearly constant.

The value R obtained when primary electrons were shooted in the centre of the scintillator ($R = 0.086$) will be marked as the *reference* value. We will use it in the next chapters for comparing with values obtained from other investigated configurations.

6.2 CENBG configuration

CENBG detector consists of a cylindrical teflon vessel with 203.2 mm radius and 240 mm height, filled with the liquid scintillator and closed with the spherical Photonis XP1806 PMT (Figure 6.11). The entrance face is covered with the strong transparent organic film Kapton with 25 micron thickness and reflective aluminum film (200 nm thickness). The aluminum is needed for reflecting back those optical photons, which

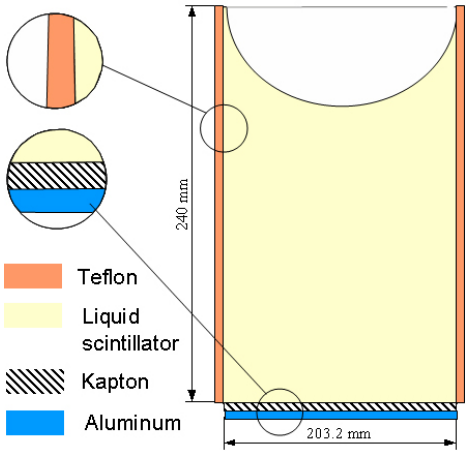

Figure 6.11: Geometry, materials and cross-section of the CENBG scintillator.

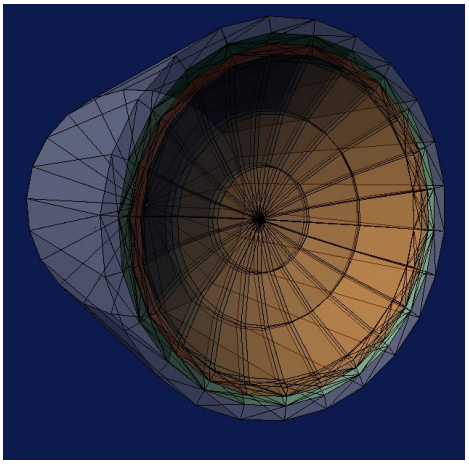

Figure 6.12: CENBG detector in Geant4 environment. The green ring is the PMT glass, the brown surface is the photocathode.

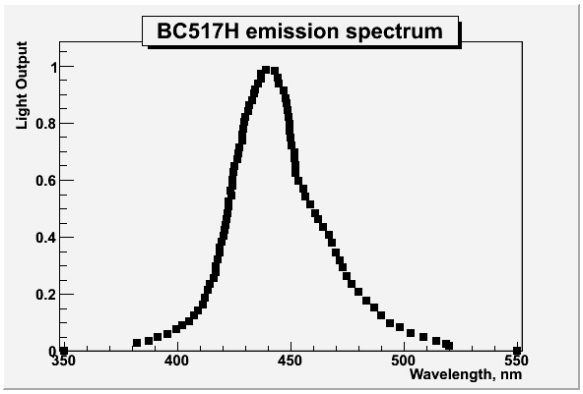

Figure 6.13: Emission spectrum of CENBG detector.

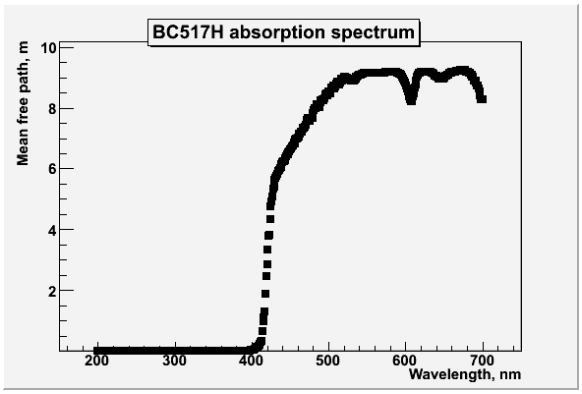

Figure 6.14: Absorption spectrum of CENBG detector.

did not reach PMT and were reflected back to the entrance. Figure 6.12 depicts the scintillator in the Geant4 environment.

The optical parameters of the CENBG scintillator were chosen from the Saint Gobain products. Reasonable approach is the liquid scintillator BC517H. Its emission spectrum (plotted in the Figure 6.13) is similar to the emission spectrum of the UCL scintillator. The absorption spectrum, however, is roughly twice so big in comparing with the UCL scintillator (pay attention to the values of Y axis in Figure 6.14). The other material properties are in Table 3. The main differences, in comparing with the UCL scintillator configuration, are the smaller light yield of the liquid scintillator - about 8600 photons per MeV, smaller absorption and the diffusive teflon wrapping.

Table 3: CENBG scintillator's material properties

Property	Value
Density	0.86 g/cc
Refractive index	1.58
Light Output, % Anthracene	52
Light Output, photons/MeV	8600
Wavelength of max. emission	425 nm
Mean free path	more than 5m

Kapton is a very strong transparent organic film needed for keeping liquid inside the teflon vessel and at the same time having thin entrance window. The wavelength dependency of PMT's quantum efficiency is used the same as in the UCL case. The dependency of teflon's reflectivity on the wavelength is shown in Figure 6.15.

After shooting a 1000 electrons with the energy 1 MeV in the centre of the scintillator, the counted value $R_{CENBGsim.} = 0.113$, while the measured value $R_{CENBGmeas.} = 0.115$. This is the only one measured result of all three configurations. The simulated result is in a good accordance with it.

6.3 ISM configuration

ISM proposed a scintillator constructed of two parts: the hexagonal base with 92 mm height and 230 mm diagonal and conical cap with 230 mm and 127 mm radia. Both parts are made of diffusive teflon vessel filled with liquid scintillator. The layer of a transparent mylar with 12 micron thickness separates scintillator material from

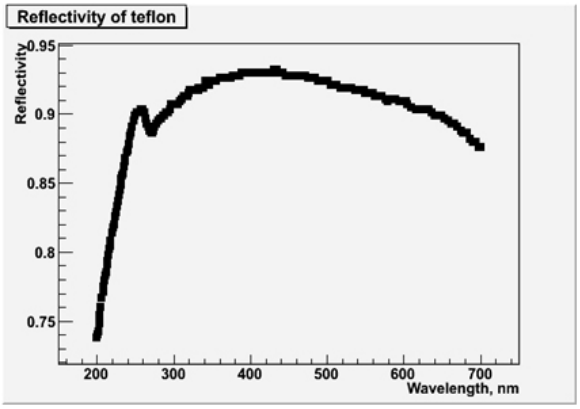

Figure 6.15: Dependency of teflon's reflectivity on the wavelength.

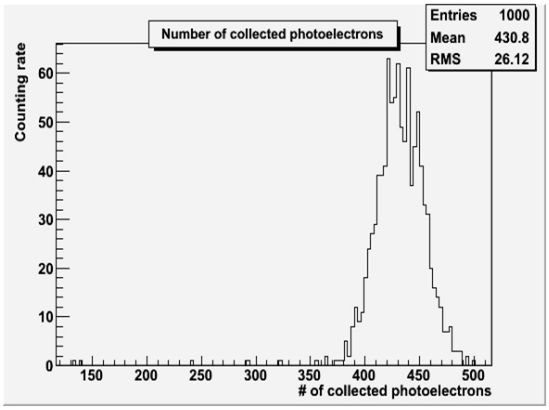

Figure 6.16: Number of photoelectrons collected in PMT in CENBG configuration.

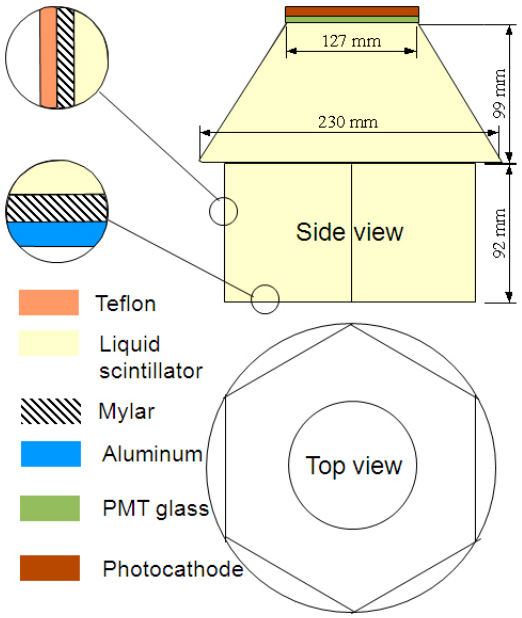

Figure 6.17: Geometry, materials and schemical views of the ISM scintillator.

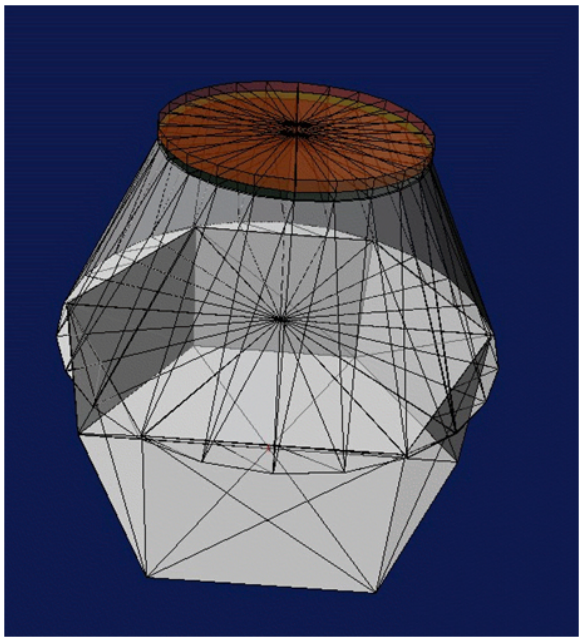

Figure 6.18: ISM detector in Geant4 environment constructed from hexagonal and conical parts. The PMT glass is marked with the green color, the photocathode is brown.

the teflon. The entrance face is covered with aluminum (22 micron thickness). The scheme of the configuration is depicted in Figure 6.17, the view of the scintillator in Geant4 visualisation environment is depicted in Figure 6.18.

For simplicity, the other scintillator properties are the same as in the case of CENBG. The absorption and emission spectra, quantum efficiency of the PMT, teflon's reflectivity, scintillator's refraction coefficient and other properties from CENBG configuration are used in ISM simulation.

Shooting of 1000 primary electrons with energy 1 MeV in the centre of the scintillator results the value of statistical contribution to energy resolution: $R_{ISM} = 0.161$.

6.4 ISM: material and wrapping analysis

We used the ISM geometry for a study of material and wrapping influence. Two alternatives of wrapping material were studied: teflon as a representation of diffusive reflector and aluminum, providing very good specular reflection.

Upper part of the ISM detector serves for guiding the light to the PMT, which has

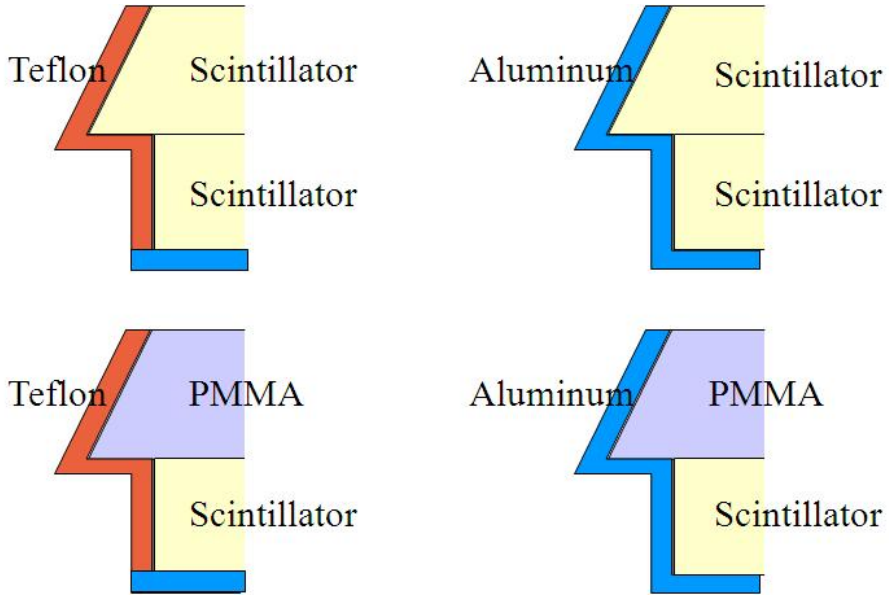

Figure 6.19: Different cases for material/wrapping analysis.

a smaller radius than the lower, hexagonal part. A good lightguide is PMMA - polymethylmethacrylate (sometimes also called acrylic glass, plexiglass or lucid). It might be used as a material for conical scintillator's part, instead of the original alternative - the liquid scintillator.

Summarizing everything what was told, we have four cases (graphically shown in Figure 6.19)

- usual configuration: liquid scintillator in the cone, teflon wrapping
- liquid scintillatore in the cone, specular (aluminum) wrapping;
- PMMA in the cone, teflon wrapping;
- PMMA in the cone, aluminum wrapping.

For clarity, results are given in the same form as it is formulated (Figure 6.20).

Comparing energy resolutions of configurations with and without PMMA, we see, that change of the liquid scintillator material to PMMA generally improves the resolution of the detector. This is due to better transparency of the PMMA in comparing with the liquid scintillator. Or, in other words, the detector's absorption is smaller.

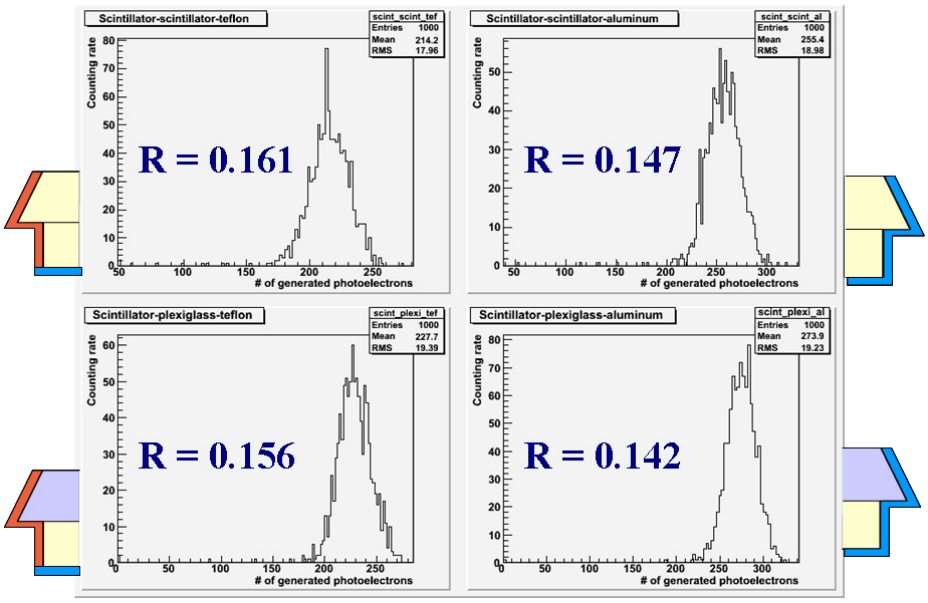

Figure 6.20: Energy resolutions for various material/wrapping configurations.

The improvement of the resolution is apparent also in the case when we change the wrapping from the diffusive to the specular. This might be due to better reflectivity of aluminum, and smaller photons' absorption in the surface.

7 Geometry of Winston cone in ISM configuration

It is obvious, that geometry do influence the light collection in scintillators. The main question is, how? To answer fully this question would be beyond the frames of this work. However, we may start here with some assumptions and ideas how to improve the light collection by choosing suitable optical-geometrical shape for scintillators.

For this purpose we will take the configuration offered by ISM, the scintillator with the hexagonal base and conical cap and modify it according to our needs. We will perform the modification of the cone to the other, more optical-based form called *Winston cone* with the hope to improve the light collection and enhance the energy resolution.

7.1 Winston cone

Winston cone is a cone made of modified parabola surface. It has three parameters: the smaller radius a_1, the bigger radius a_2 and the length of the cone L (Figure 7.1). The formula of the parabola with a focus f is

$$y^2 = 4f(x + f). \tag{7.1}$$

The focus f can be expressed through the parameters of Winston cone:

$$f = a_1(1 + sin(\theta)), \tag{7.2}$$

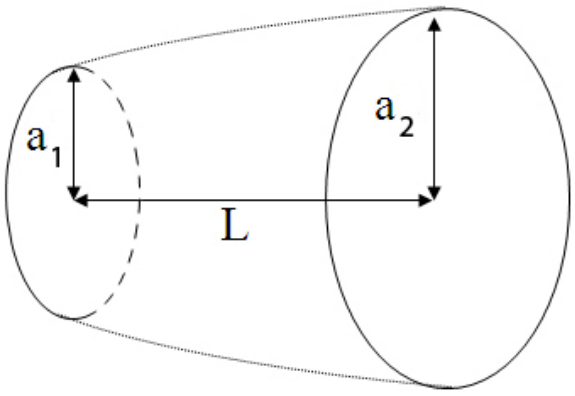

Figure 7.1: Winston cone with main parameters: smaller radius a_1, bigger radius a_2, length L.

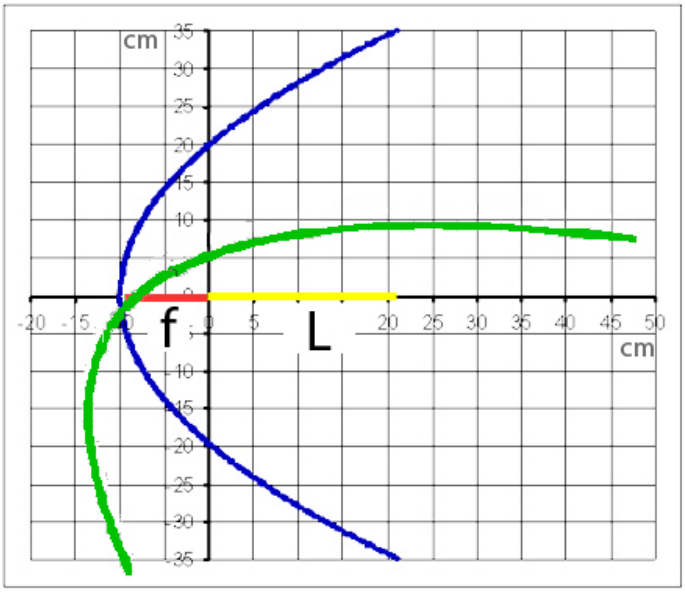

Figure 7.2: Blue: parabola with the focus f (red line). Green: rotated and translated parabola. Yellow: the length of the Winston cone L.

where

$$sin(\theta) = \frac{a_1}{a_2}. \tag{7.3}$$

The next step is to provide the translation and the rotation of the parabola (Figure 7.2):

$$\begin{pmatrix} x' \\ y' \end{pmatrix} = \begin{pmatrix} cos\,(\theta) & sin\,(\theta) \\ -sin\,(\theta) & cos\,(\theta) \end{pmatrix} \begin{pmatrix} x \\ y \end{pmatrix} - \begin{pmatrix} 0 \\ a_1 \end{pmatrix}. \tag{7.4}$$

The length L is related with the radia a_1 and a_2:

$$L = (a_1 + a_2)\, cot\,(\theta)\,. \tag{7.5}$$

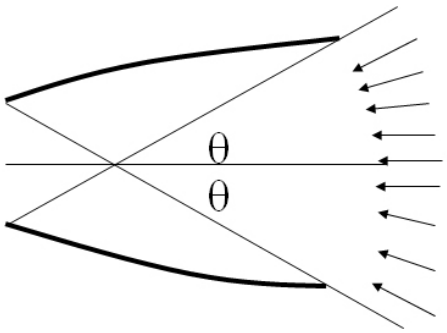

Figure 7.3: All light entering the cone with angle $< \theta$ will fall into the smaller end of the cone.

Winston cone has following optical properties: All photons, entering the cone through the bigger end with radius a_2 with the incident angle smaller than θ, directly or with one reflection will reach the smaller end with radius a_1 (Figure 7.3). However, if the incident angle will be bigger than θ, the photons will be reflected back. In the next chapter we will describe how to turn these properties to our benefit and improve the energy resolution of ISM configuration.

7.2 Application of Winston cone in ISM configuration

The conical part in original ISM configuration has two major disadvantages. The first one is its material. 10 cm of liquid scintillator is accepted as an optimal thickness for electron and gamma registration. The thickness of the hexagonal part is enough to satisfy this condition, thus, the material of the conical part may be replaced by the other, more transparent one. Then more optical photons will survive the absorption. We have confirmed it already in chapter 6.4.

The second disadvantage comes from the arrangement of more such scintillators to a plane. The shape of the cone must be corrected in such way, that two (and more) hexagonal parts could be placed side by side, making a wall of scintillators. In other words, the edges of the cone must be cutted off. We will apply those two requirements for the Winston cone, which will eventually replace the normal cone in ISM configuration. One more requirement comes out from the optics of Winston cone: the reflective surface must be specular, not diffusive.

Recapitulating of what was told we have:

- The material of Winston cone must be more transparent than the liquid scintillator. In the simulation we will use PMMA, which is known as a very good lightguiding material.
- The edges of Winston cone must be cutted off.
- The surface of Winston cone must be specular.

We adopt the Winston cone for the ISM hexagonal basement. The bigger radius a_2 will be the same as the radius of hexagon, 230 mm. The smaller radius a_1 will be

the radius of the PMT, 127 mm. Magnitudes of radia define the length L, which, according to equations (7.5) and (7.3) is 269 mm. If we cut the piece of the rotated and translated parabola restricted by the length L (Figure 7.2) and rotate it around the X axis, then the rotation surface will be Winston cone, depicted in Figure 7.1.

All this gives a new composition of the detector, depicted in Figure 7.4. Its width remains the same as before, 230 mm, the height is 361 mm instead of former 191.

After a closer look in cutted Winston cone (Figure 7.4) we may notice, that the bottom part is "much more hexagonal than conical". Thus, we may use the first 10 cm of it as a scintillator, and the height of the whole detector decreases from 361 mm to 269 mm. Figure 7.5 graphically represents this idea.

The benefits of Winston cone-based lightguide are:

- Part of the light, falling into the Winston cone at the angle smaller than θ, will undergo zero or one reflection. The surviving probability of optical photons will be bigger, and bigger fraction of them will reach the photocathode.
- The light reflected back in scintillator could interact with its diffusive surface.

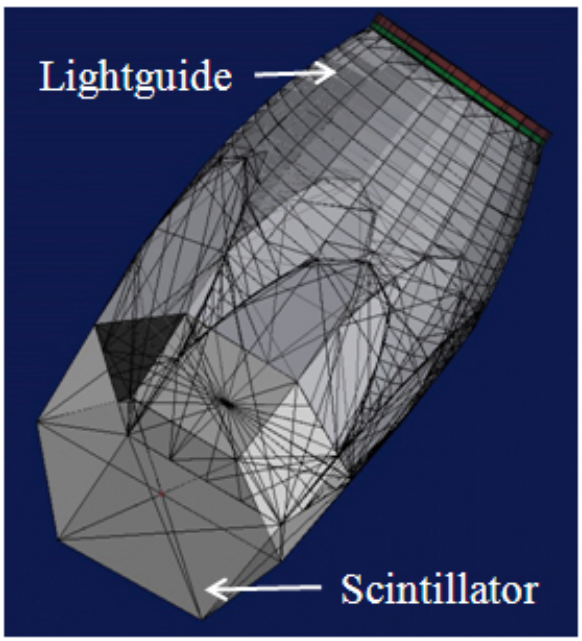

Figure 7.4: ISM configuration with cutted Winston cone instead of normal one.

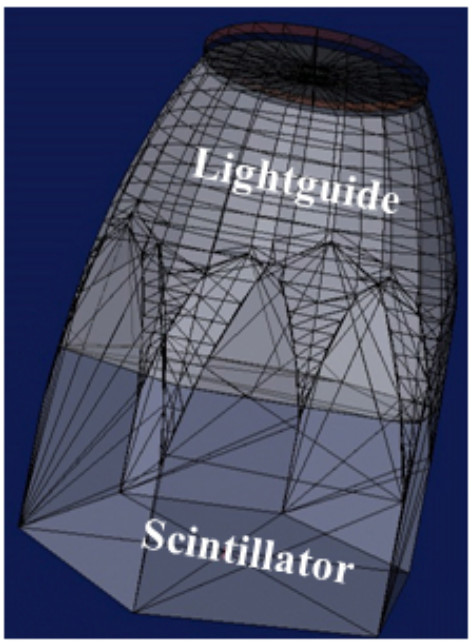

Figure 7.5: Final version of the ISM configuration modification. Cutted Winston cone, where first 10 cm of it are the liquid scintillator, the rest is plexiglass.

There would be a chance to return the light back into the Winston cone with the angle smaller than θ.

7.3 Material and wrapping analysis of modified ISM configuration

In the previous chapter we have written major ideas how to modify the shape of the lightguide in the ISM configuration in order to get better energy resolution. In the chapter 6.4 we have seen the influence of material and wrapping on the resolution. Here we will present the results of four tested combinations of modified ISM configuration.

The upper part (lightguide) remains unchanged: PMMA material in Winston cone and specular aluminum wrapping around it. The hexagonal part has the following options:

1. liquid scintillator material with aluminum wrapping;
2. liquid scintillator material with diffusive teflon wrapping;
3. plastic scintillator with aluminum wrapping;

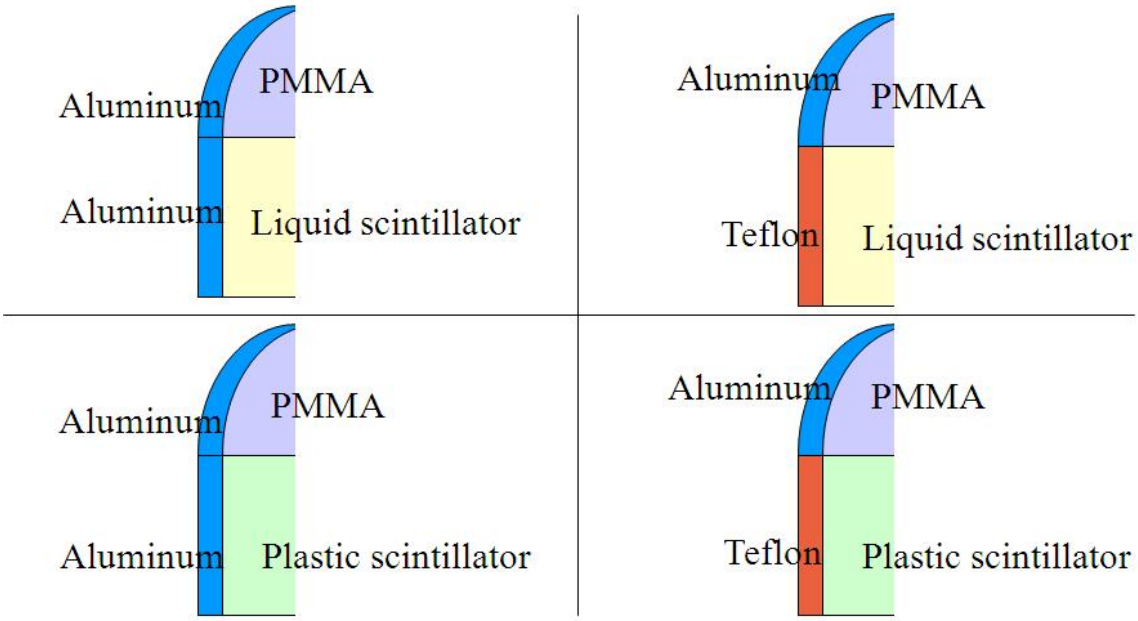

Figure 7.6: Different cases in material/wrapping analysis in modified ISM configuration.

4. plastic scintillator with teflon wrapping.

Figure 7.6 represents the idea more clearly. Plastic scintillator material is introduced because of its better light yield.

Results confirm the expected improvement of the energy resolution (Figure 7.7). After replacing the normal cone with Winston cone, the energy resolution improved from 0.161 to 0.156. Changes of wrapping and material (aluminum instead of teflon and plastic scintillator instead of liquid) bring the R value to 0.148.

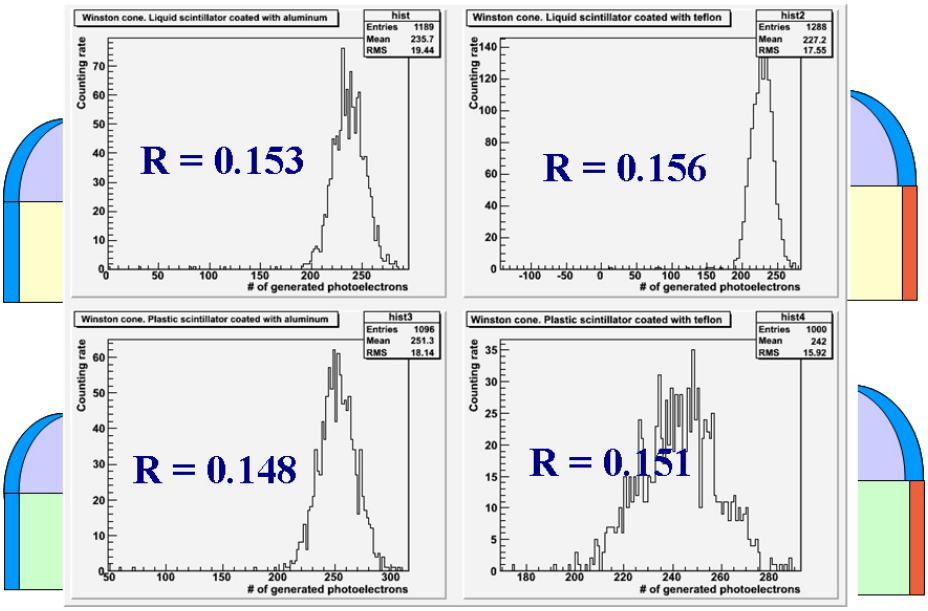

Figure 7.7: Results of four tested combinations of modified ISM configuration.

8 Conclusions

Four different detector configurations have been studied. Their performance have been estimated using Monte Carlo method with Geant4 simulation toolkit. The statistical contribution to energy resolution R was evaluated for different scintillator materials (liquid and plastic), shapes and wrappings.

UCL detector has the best value of R (0.086), but due to small size is insensitivee for gamma particles. Its value of R is 0.086. One- and two-dimensional scans showed, that the energy resolution depends on the point where electron beam incidents detector's entrance face. The value of R gradually rises when the incident point moves towards the edge of the detector. R is nearly constant along the detectors edges.

CENBG's configuration simulations are very important in the sence of comparing simulation results with measured data. $R_{CENBGsim} = 0.113$, which is in excellent agreement with the experimental value $R_{CENBGmeas} = 0.115$. This signals the good reliability of simulations in further calorimeter's developement and design. However, more experimental data are awaited from collaborators to be compared with other simulations presented in the thesis.

ISM configuration's studies showes the significance of the right choice of wrapping and lightguide's material. The combination of the most transparent lightguide and best wrapping's reflectivity reduces the value of R from former 0.161 to 0.142. Optical-based lightguide's shape contributes to the improvement of the energy resolution too. Introduction of Winston cone reduces the value of R from 0.161 to 0.156. Combination with more transparent scintillation material and wrapping with better reflectivity brings this value to 0.148.

Although the simulations need experimental confirmation, the presented study provides general rules, which may be applied in SuperNEMO calorimeter design.

References

[1] Geant4: Physics Reference Manual (14 December, 2007).
http://geant4.web.cern.ch/geant4/UserDocumentation/UsersGuides/PhysicsReferenceManual/html/PhysicsReferenceManual.html

[2] Facilities and Methods: Geant4 - A Simulation Toolkit. J.Allison, Nuclear Physics News, Volume 17 Issue 2. Taylor & Francis (2007).

[3] First results of the search for neutrinoless double-beta decay with the NEMO-3 detector. R. Arnold et al., PRL 95, 182302 (2005).

[4] Leo, W. R. (1992) Techniques for Nuclear and Particle Physics Experiments: A How-To Approach. Berlin: Springer-Verlag.

[5] Proposal for an R&D program for a double beta decay experiment sensitive to a 50 meV neutrino effective mass. SuperNEMO collaboration. (March 9, 2005).

[6] Search for Neutrinoless Double Beta Decay with NEMO 3 and SuperNEMO. S. Söldner-Rembold, Journal of Physics: Conference Series 110 (2008) 082019.

[7] Technical design and performance of the NEMO-3 detector. R. Arnold et al., Nucl. Instrum. Meth. A536 (2005) 79, arXiv:physics/0402115

[8] Vikuiti reflective films
http://solutions.3m.com/wps/portal/3M/en_US/Vikuiti1/BrandProducts/main/productliterature/backlightreflectorfilms/

[9] R. Winston. Light Collection within the Framework of Geometrical Optics. J. Opt. Soc. Am. 60, 245- (1970)

[10] Клапдор-Клайнгротхаус, Г. В., Штаудт, А.(1997) Неускорительная физика элементарных частиц. Наука. Физматлит, Москва.